FULL PAPER

Magnetic Resonance in Medicine 000:000–000 (2010)

Arterial Transit Time Effects in Pulsed Arterial Spin Labeling CBF Mapping: Insight From a PET and MR Study in Normal Human Subjects

Maolin Qiu,[1*] R. Paul Maguire,[4] Jagriti Arora,[1] Beata Planeta-Wilson,[1] David Weinzimmer,[1] Jinghua Wang,[1] Yuenan Wang,[2] Hyeonjin Kim,[1] Nallakkandi Rajeevan,[1] Yiyun Huang,[1] Richard E. Carson,[1,2] and R. Todd Constable[1,2,3]

Arterial transit time (ATT), a key parameter required to calculate absolute cerebral blood flow in arterial spin labeling (ASL), is subject to much uncertainty. In this study, ASL ATTs were estimated on a per-voxel basis using data measured by both ASL and positron emission tomography in the same subjects. The mean ATT increased by 260 ± 20 (standard error of the mean) ms when the imaging slab shifted downwards by 54 mm, and increased from 630 ± 30 to 1220 ± 30 ms for the first slice, with an increase of 610 ± 20 ms over a four-slice slab when the gap between the imaging and labeling slab increased from 20 to 74 mm. When the per-slice ATTs were employed in ASL cerebral blood flow quantification and the in-slice ATT variations ignored, regional cerebral blood flow could be significantly different from the positron emission tomography measures. ATT also decreased with focal activation by the same amount for both visual and motor tasks (~80 ms). These results provide a quantitative relationship between ATT and the ASL imaging geometry and yield an assessment of the assumptions commonly used in ASL imaging. These findings should be considered in the interpretation of, and comparisons between, different ASL-based cerebral blood flow studies. The results also provide spatially specific ATT data that may aid in optimizing the ASL imaging parameters. Magn Reson Med 00:000–000, 2010. ©2009 Wiley-Liss, Inc.

Key words: arterial transit time; cerebral blood flow; positron emission tomography; pulsed arterial spin labeling; brain vasculature

Significant efforts have been made to improve the accuracy of absolute cerebral blood flow (CBF) measurements estimated by pulsed arterial spin labeling (ASL) MRI. To improve the inversion profile and the labeling efficiency, adiabatic or hypersecant pulses and other variants have been proposed (1–4). To overcome the signal dampening due to the off-resonance effect of the inversion radiofrequency (RF) pulse, separate coils for labeling and detection have been employed (5–9). Measurement of the arterial blood proton density was suggested to minimize the nonuniformity of the brain tissue-blood partition coefficient (λ) (10), and methods have been presented to reduce the sensitivity of CBF quantification to arterial transit time (ATT) effects (contamination from intravascular arterial blood water) in CBF quantification (11–13).

In ASL, water in the arteries is magnetically labeled, and when it reaches the capillary bed and exchanges with the extravascular water, the labeled water induces changes in local magnetization relative to the case in which the arterial water is undisturbed. These changes are detectable by MRI and such images of the intensity changes are perfusion weighted. Absolute CBF values can be calculated based on these perfusion-weighted intensity changes. ATTs, however, are one of the key phenomena that affect the calculation of the absolute CBF from the image intensity differences. In ASL, ATT refers to the time it takes the arterial blood to travel from the labeling site to the capillaries in the tissue being imaged. By definition, the ATT sets a minimum delay time between the RF labeling and data acquisition. The ATT must be known in order to calculate absolute CBF. The effect of uncertainty in the ATT on CBF quantification has been actively investigated by a number of authors (13–19). Several methods have been proposed to measure ATT values using the ASL sequence either with arterial blood flow crusher gradients (14,18) or by varying the postlabeling delay times (13,15,17,19,20). Since the ATT values in ASL are dependent on the geometric setup, i.e., factors such as the slice thickness and orientation, imaging location, and the gap between labeling and imaging slabs, the ideal acquisition should include a measure of the voxelwise ATTs in the ASL imaging protocol. In practice this is not done because all of the available methods for measuring ATTs are very time consuming and suffer from low signal-to-noise ratio and contamination from intravascular signals, and hence the measurements tend to be inaccurate.

Three practical approaches have been used to address uncertainties in the ATT: first, empiric per-slice ATT values are used from other ATT studies; second, it has

[1]Department of Diagnostic Radiology, Yale University School of Medicine, New Haven, Connecticut, USA.

[2]Department of Biomedical Engineering, Yale University School of Medicine, New Haven, Connecticut, USA.

[3]Department of Neurosurgery, Yale University School of Medicine, New Haven, Connecticut, USA.

[4]Pfizer Global R&D, New London, Connecticut, USA.

Current address for R. Paul Maguire: Novartis Institutes for BioMedical Research, WKL-135.1.74, Klybeckstrasse 141, CH-4057 Basel, Switzerland. E-mail: paul.maguire@novartis.com.

Grant sponsor: National Institutes of Health; Grant numbers: NS047605, NS051622, and NS052344.

*Correspondence to: Maolin Qiu, Ph.D., Yale University School of Medicine, Department of Diagnostic Radiology, MRRC, The Anlyan Center, N127, 300 Cedar Street, New Haven, CT 06520-2048. E-mail: maolin.qiu@yale.edu

Received 13 March 2009; revised 26 August 2009; accepted 26 August 2009.

DOI 10.1002/mrm.22218
Published online in Wiley InterScience (www.interscience.wiley.com).

been suggested that when multiple slices are acquired in an ascending order as in quantitative imaging of perfusion using a single subtraction II (QUIPSS II) (10,12), the mean ATT for each slice coincides with the postlabeling delay time for the same slice, and CBF measurements can be scaled accordingly; and third, ASL imaging sequences have been modified to incorporate the ATT term but nonlinear equations have been solved to yield both the CBF and ATT (21–25). This last approach has the same drawbacks as measuring ATTs by varying the postlabeling delay times.

This work examines several issues related to the ATTs in ASL by taking advantage of the CBF measures obtained using [^{15}O]water positron emission tomography (PET), which is considered the gold standard for measuring CBF. Absolute CBF values on a per-voxel basis were obtained using PET, and MR measures of perfusion-induced changes in signal intensity, proton density, and the T_1s were obtained in the same subjects. These data allowed for a direct calculation of the ATT value for any voxel that was included in both the PET and ASL acquisitions. A variety of imaging geometries are used in ASL imaging to measure CBF by investigators from different research groups, yet the dependence of the ATT values upon the imaging geometry is assumed to be insignificant and is therefore not taken into consideration in CBF quantification. This work addresses the impact of geometrical issues on the ATT values required by ASL and examines the impact of the ATT values on CBF measured using ASL due to different geometric setups. First, fusing both PET and MRI acquisitions from the same subjects allowed us to investigate the extent to which the per-slice ATT values depend upon the location of the imaging slab and the gap between the imaging and labeling volumes; second, when the ATT values on a per-slice basis are empirically assumed or borrowed from the literature, differences in the exact image acquisition parameters and geometries are often ignored at the expense of accuracy, and this work examines the significance of within-slice variations in ATT; third, activation-induced changes in ATT were quantified within sensorimotor and visual regions of interest (ROIs) to provide insight into the errors that arise in CBF quantification due to task-induced ATT changes that are ignored in practice.

Clarification of these issues not only reveals the quantitative relationship between the ATTs and the ASL imaging geometry but also allows an evaluation of the ATT assumptions commonly used. The findings provide a framework for the interpretation of and comparison between ASL-based CBF studies. The spatially specific ATT data may also be useful in choosing optimal ASL imaging parameters and aid in minimizing errors in absolute CBF quantification.

MATERIALS AND METHODS

Subjects

Fourteen healthy consenting subjects (all males, average age 27 ± 6 years) were recruited to participate in a protocol approved by the Institutional Review Board of Yale University School of Medicine. All the subjects underwent two MRI sessions at the Yale University Magnetic Resonance Research Center (and the data from the two sessions were averaged) and one PET session at the Yale University Positron Emission Tomography Center. All three visits were scheduled on different days, maximally 4 weeks apart, typically in the order MR-PET-MR.

Magnetic Resonance Imaging

Magnetic resonance imaging data were acquired on a 3-T whole-body scanner Trio (Siemens Medical Systems, Erlangen, Germany) with a circularly polarized head coil. Pulsed ASL (PASL) imaging was used to measure perfusion-induced changes in image signal intensity during the resting state or in the presence of sensorimotor (finger tapping) or visual stimulation. The QUIPSS PASL sequence was modified from the EPISTAR (echo-planar imaging with signal targeting using alternating radio frequency) sequence by adding a train of thin-slice saturation RF pulses, which were applied at the postlabeling delay inversion time $(TI)_1 = 700$ ms after the inversion RF pulse to control the bolus delivery and suppress the intravascular signal from large vessels (12). Interleaved labeling and control images were acquired using a gradient echo-planar imaging sequence. A slab-selective (100 mm) hypersecant inversion RF pulse was used for ASL. The RF pulse was applied to a slab 20 mm inferior to the imaging slab. As a control, the same RF pulse was applied to a slab 20 mm superior to the imaging slab. In order to obtain whole brain coverage, ASL data were collected separately for the upper and lower parts of the brain. For each part, 10 anterior commissure-posterior commissure (AC-PC) aligned slices were acquired from inferior to superior in an ascending order. For the sensorimotor task, the imaging slab was positioned on the upper part of the brain, with the lowest slice passing through the AC-PC line; for visual stimulation, the imaging slab was positioned on the lower part of the brain, with the 7th slice from the bottom passing through the AC-PC line. The ASL acquisition parameters were field of view = 240 × 256 mm^2; matrix = 60 × 64; and bandwidth = 2298 Hz/pixel. We define the effective slice thickness as the imaging slice thickness plus the interslice gap; slice thickness = 6 mm, interslice gap = 3 mm, effective slice thickness of 9 mm. The pulse repetition time (TR) = 2000 ms; the echo time = 20 ms. Acquisition of each slice took approximately 55 ms; therefore, the postlabeling TI for each slice i, i = 1, 2, … , 10, $TI(i) = 1400 + 55 \times (i - 1)$ ms. A bipolar gradient of encoding velocity $V_{enc} = 5$ cm/sec was applied to the imaging slices to suppress the signal contamination from the labeled arterial water within large vessels. To reduce the variability in the ATT estimation, the proton-density-weighted image and the apparent T_1 map T_{1app} were estimated for both upper and lower parts of the brain. Proton-density-weighted images were collected using the same perfusion sequence, except for the following changes: TR was set to 8000 ms, the delay time was set to 0 ms, and the TI was set to 6050 ms. The T_{1app} mapping data were acquired using an ultrafast Look-Locker echo-planar imaging T_1 mapping sequence (26). Two additional acquisitions were acquired to aid in multisubject registration. First, a high-resolution whole-brain

three-dimensional (3D) structure image was acquired for each subject using magnetization prepared rapid acquisition with gradient-echo imaging, with the following settings: 160 sagittal slices with field of view = 256 × 256 mm^2, voxel size = 1 × 1 × 1 mm^3, TR = 1500 ms, TI = 800 ms, echo time = 2.83 ms, flip angle 15°, and one average. Next, two sets of multislice two-dimensional T_1-weighted images, each for one part of the brain, were acquired during each MR session, using the same slice positions as the perfusion-weighted images, with the following settings: field of view = 256 × 256 mm^2, in-plane resolution 1 × 1 mm^2, TR = 300 ms, echo time = 3.69 ms, flip angle 60°, and two averages.

[^{15}O]Water PET Imaging

The PET scan session required insertion of an arterial catheter for the purpose of drawing blood to measure the input function. A catheter was placed in the subject's radial artery (nondominant side), after establishing an adequate ulnar and radial arterial supply to the hand, using the Allen test. In all but one subject, the arterial line was placed in the left arm. PET imaging was performed using a high-resolution research tomograph (Siemens, Knoxville, TN), which acquires 207 slices (1.2 mm slice separation) with reconstructed image resolution of ~2.5 mm. Subjects were positioned in the camera head first, supine with their arms by their sides. Each subject's head was centered in the field of view and immobilized using a chin strap. A 6 min transmission scan was acquired for attenuation correction. Twelve bolus injections (20-sec duration) of 20 mCi of [^{15}O]water each were administered through an i.v. line at intervals of 10 min, using an infusion pump. List mode data were acquired on the high-resolution research tomograph for each scan. Acquisition of high-resolution research tomograph list mode data began shortly before each injection. Simultaneously, the arterial input function was measured with an automated blood-counting system (phosphate-buffered saline-101; Veenstra Instruments, Joure, the Netherlands), using a continuous withdrawal system with a peristaltic pump (4 mL/min). The radioactivity in whole blood was measured with a calibrated radioactivity monitor. The total blood withdrawal per injection was <20 mL.

Task Paradigm

During each run in an MRI session, the presentation of tasks, either sensorimotor or visual, had a pattern of "off-on-off-on-off", each "off/on" period lasting for 60 sec, and for each run the scan time was 5 min. The sensorimotor task was a visually guided unilateral finger tapping. The visual clue was projected to a screen that the subject could see through a mirror system. A small white fixation crosshair "+" was presented against a black background at the center of the screen during the control periods. For each run, an arrow remained either on the left or on right side of the fixation crosshair, assigning the hand to be used, and a number (1 to 4) was presented in a randomized order at a rate of 3 Hz, notifying the subjects of the tapping finger. Each MRI session consisted of four sensorimotor runs, and for each run, the hand the subject used to perform the finger-tapping during was randomly chosen. Visual stimulation used an 8-Hz reversely flashing full-field black-white checkerboard with the horizontal and vertical extent ~16 and 12°, respectively. During the visual rest intervals, the subjects fixated on a small white fixation crosshair "+" presented against a black background. Four visual runs were performed during each MRI session. Exactly the same imaging protocol was repeated during the subject's second MRI visit.

For the PET sessions, subjects were asked to perform visual and motor tasks during the 12 [^{15}O]water scans. The task acquisition (performed in random order) consists of four baseline resting-state central fixation injections, four scans during the flashing full-field checkerboard visual stimulation, and four scans during the visually cued finger-tapping paradigm with the injection in the arm opposite to the intra-arterial line placement (right arm for 13 subjects). The position and size of the display screens were chosen to provide a solid angle of viewing closely matched across the PET and MR sessions. The presentation of tasks had the pattern of "off-on-off-on-off", each for 60 sec (total of 5 min), which was identical to that in the ASL session. Due to the nature of PET, the timing of scans was different. Each of the task sessions began 1 min before injection time, during which time the subject performed central fixation. This was followed by full-field flashing checkerboard or alternating fixation/finger tapping blocks, which began coincident in time with the [^{15}O]water injection. Since the critical period for PET CBF measurements is in the first 10-15 sec following bolus arrival in the brain (27), and the relevant data acquisition time was 90 sec, the second presentation of stimulus had no effect on the data but was included to match the stimulus presentation to that of the MR sessions.

Data Processing

ASL Perfusion-Weighted Images

Perfusion-weighted and the proton-density weighted images were motion-corrected using the Statistical Parametric Mapping package (SPM99) via a six-parameter rigid-body transformation. Time series of the perfusion-weighted images were obtained by pairwise "surround" subtraction between interleaved label and control pairs for either the resting state or task-performing conditions, resulting in a temporal resolution of 2TR (28–30). Perfusion-induced difference maps (ΔM) were calculated by averaging all the difference images in the time series for each condition. The mean image of the motion-corrected proton density images (M_0) was estimated by averaging multiple acquisitions.

PET CBF Quantification

Motion correction of PET images was performed in two steps. First, for each injection, images without attenuation and scatter correction were reconstructed. Then, all scans were registered to the first scan using FSL 3.2 (Analysis Group, FMRIB, Oxford, UK) with a six-parameter rigid transformation. This step produced a motion correction file that was applied in the second-phase of reconstruction. This reconstruction step incorporates the

motion information directly so that the transmission data are properly aligned with the emission counts (31). The final PET images for each injection were accumulated for 90 sec following arrival of the tracer in the brain, determined by examination of the whole-head count rate curve. Maps of the average radioactivity concentration were reconstructed with corrections for measured attenuation, normalization, motion, scatter, and dead time.

The blood radioactivity data were corrected for background, dead time, sensitivity, and dispersion (between the catheter and the detector). Time shifts (mean = −0.333 min, standard deviation = 0.074 min) between blood and brain data were determined by aligning scanner count rate data (measured once per second) to the blood data (32), specifically, a 15-sec period of whole-brain count-rate data starting ~5 sec before tracer arrival was fitted to the one-compartment model with two parameters: whole-slice CBF and time shift. Tissue clearance was assumed to be negligible during this period. CBF images were produced on a pixel-by-pixel basis by the autoradiographic method (33), using an assumed value of the water partition coefficient (λ) of 0.9 mL/g and a correction for average brain density of 1.05 g/mL.

Intersubject Data Integration

A standard whole-brain template defined by the Montreal Neurological Institute (MNI; 1 mm) was used for subject spatial normalization of the group data. Registration of multiple subject data and group analyses were carried out using the BioimageSuite software package bioimagesuite.org (34) for both PASL and PET images. Two transformations were performed to allow multiple subject integration: first, a linear transformation was estimated by coregistering the subject's upper or lower set of multislice two-dimensional T_1-weighted images to the high-resolution 3D anatomic image of the same subject, and this was then used to transform the individual maps of both the resting state and task-induced data to the high-resolution 3D anatomic space of that subject; second, a nonlinear transformation was used to coregister the high-resolution 3D anatomic image of each subject to the common brain template, which enabled warping of all the transformed maps of a subject to a common brain space. Trilinear interpolation was employed for image regridding in the common 3D space. All group analysis was performed in the common space. Voxelwise contrasts between conditions were estimated using the pooled-subject data to test the null hypothesis.

For each MR session, the resting state data of the upper part of the brain were estimated from the images collected during the resting periods of the sensorimotor stimulation paradigm and those of the lower part from the resting periods of the visual paradigm. The maps of the two parts were normalized to the common brain template separately. If in the common space there was an overlap of the data from these two volumes, the average voxel value was used in the overlap region. Individual subject PET data covering the whole brain was first registered to the subject's structural 3D MR image using a seven-parameter linear registration (the 7th parameter allowed for slight differences in physical scale between PET and MR), and these data were then transformed into the common space in the same manner as for the MR data.

ATT Mapping

Given the perfusion-induced intensity changes in ASL images ΔM, the proton-density-weighted image M_0, the apparent T_1 T_{1app}, and the CBF data measured by PET (f_{PET}), by rearranging the terms of the following equation commonly used for CBF calculation in PASL:

$$\Delta M(\mathrm{TI}) = M^{\mathrm{ctrl}}(\mathrm{TI}) - M^{\mathrm{label}}(\mathrm{TI}) = \frac{2cfM_0(\mathrm{TI}-\tau_a)}{\lambda} e^{-\mathrm{TI}/T_{1a}} \quad [1]$$

and assuming CBF was measured using PET, $f = f_{PET}$, the ATT (τ_a) can be calculated based on the following equations:

$$\tau_a = \mathrm{TI} - \frac{\lambda \Delta M(\mathrm{TI}) e^{\mathrm{TI}/T_{1a}}}{2cf_{\mathrm{PET}}M_0} \quad [2]$$

in which λ is the tissue-blood partition coefficient for water; T_{1a} is the T_1 for the arterial blood, and

$$c = \alpha_\pi \frac{1 - e^{-(\mathrm{TI}-\tau_a)(1/T_{1\mathrm{app}} - 1/T_{1a})}}{(\mathrm{TI}-\tau_a)(1/T_{1\mathrm{app}} - 1/T_{1a})} \quad [3]$$

is the correction factor, which accounts for the magnetization exchange between intravascular and extravascular space in the capillary bed; α_π is the ASL efficiency of the RF pulse. An iterative algorithm was employed to estimate τ_a (see the Appendix for more details).

All the PET and ASL data were transformed to the common MNI space, and therefore the ATT values were also calculated for each individual dataset in the common space. Across-subject variability was minimized at scan prescription by locating slices based on the AC-PC landmark; after transformation to the common MNI brain space, the ASL acquisition order of each voxel and the TI associated with each voxel could be different. For each voxel, information regarding the acquisition slice number was stored in the geometric information image for each subject, which enabled the calculation of individual ATT values in the common space before performing group analysis. To register the ASL slice information in the common space, for each individual ASL dataset, a 3D image was created and each voxel was assigned a number (1 to 10) indicating the acquisition order. This 3D image contained the same geometric information as M_0 and it was transformed to the common space using the same transformations as applied to M_0. This transformed image provided information about when a voxel was acquired and thus the associated TI.

ROI

Sensorimotor and visual brain ROI were defined in the common reference space based on the task-induced changes in PET CBF maps. Multiple voxel comparison correction was considered in the definition of the sensorimotor and visual ROIs ($P < 0.05$, corrected) (35). The size of the sensorimotor ROI was ~2430 mm^3 and that of

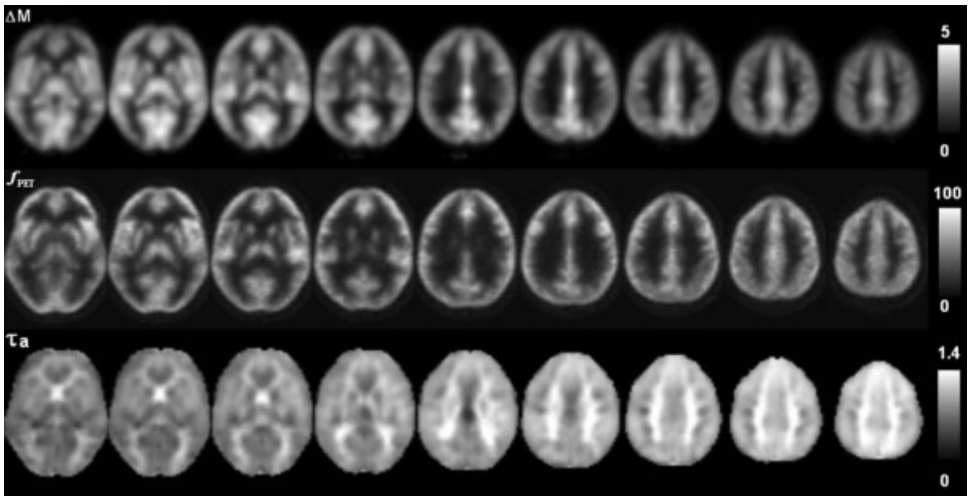

FIG. 1. Group average data. Nine slices (resliced) from the upper acquisition slab show the perfusion-induced signal intensity changes in ASL images (top, a.u.), CBF map measured by [^{15}O]water PET (middle, mL/100 g/min), and the ATT map (bottom, seconds) estimated on a per-voxel basis. As shown in the ATT map, a brain mask was generated by thresholding the group average blood oxygen level dependent (BOLD) images to excluded the ATT values from those regions where apparent image distortion and signal dropout exist, especially in the inferior slices, as shown in Fig. 2.

the visual ROI ~2970 mm^3. These ROIs (Fig. 5) were used to evaluate the ATT in both the resting and the activated states and to examine the changes in the ATT due to activation.

RESULTS

The group average of the perfusion-induced changes in ASL signal intensity, the CBF maps measured by PET, and the ATT maps estimated are shown in Fig. 1 for the upper part of the brain and in Fig. 2 for the lower part. These are pooled-subject data and the images shown are composites in the common space. The maximum ATT values in the upper and lower parts of the brain were approximately 1.4 and 1.8 sec, respectively.

After the ATT values were estimated on a per voxel basis, the in-slice mean ATT values were calculated for each subject in terms of the original ASL acquisition order. Group analysis of the in-slice mean ATT values was performed for both upper and lower parts of the brain. The in-slice spatial SD of the ATT values was also estimated as a measure of the in-slice ATT spatial variability, which is often ignored in quantitative ASL CBF applications. These results are also shown in Table 1a and b. For the upper part of the brain, the mean ATT value is 630 ± 30 (standard error of the mean) ms for the 1st slice and 1120 ± 40 ms for the 10th slice when the spacing between the labeling and imaging slabs was 20 mm (Table 1a). Linear regression shows excellent goodness of fit, with $R^2 = 0.95$, and an ATT increase of 63.5 ms per slice was observed when the effective slice thickness was 9 mm (Fig. 3). For the lower part of the brain, the mean ATT value is 970 ± 20 ms for the 1st slice and 1430 ± 40 ms for the 10th slice (Table 1b). Linear regression also shows an excellent goodness of fit, with $R^2 = 0.95$, and an ATT increase of 50.4 ms per slice was observed.

Segmentation of the brain into gray and white matter was performed in the common MNI space based on T_1-weighted anatomic images, and the mean in-slice ATT

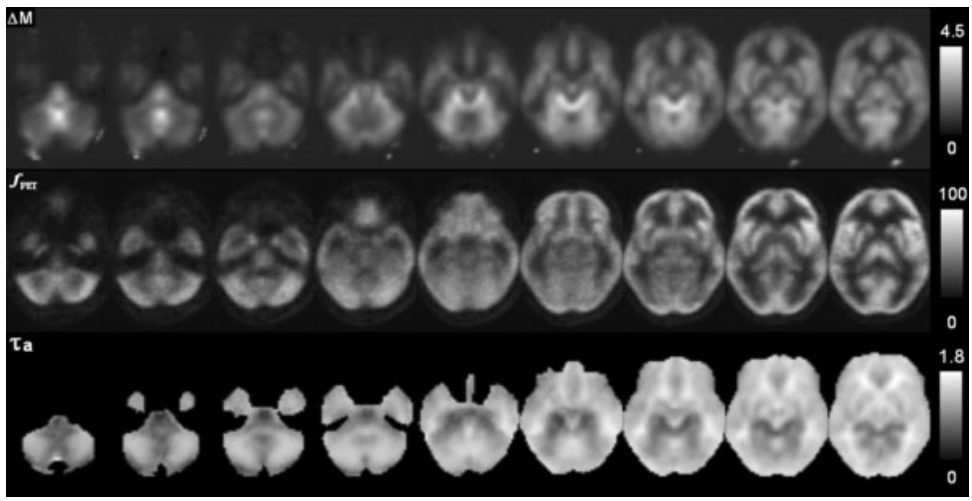

FIG. 2. Group average data. Nine slices (resliced) from the lower acquisition slab show the perfusion-induced signal intensity changes in ASL images (top, a.u.), CBF map measured by [^{15}O]water PET (middle, mL/100 g/min), and the ATT map (bottom, seconds) estimated on a per-voxel basis.

Table 1
In-slice Mean ATT and the In-Slice ATT Spatial Variability were Calculated in the Upper Acquisition Slab **(a)** and Lower Slab **(b)** of the Brain. For Either Section, the In-Slice Mean ATT Values are Listed in the 2nd Column from Left. The Across-Subject Variability of the Mean ATT Values is in the 3rd Column. The Last Two Columns Show the In-Slice Mean ATT Values for the Gray and White Matter, Respectively

	In-slice mean ATT[a] ± SD	ATT spatial variability ± SD	Mean GM ATT[a] ± SD	Mean WM ATT[a] ± SD
a: Upper slice #				
1	630 ± 150	220 ± 30	620 ± 130	640 ± 150
2	670 ± 150	210 ± 30	660 ± 140	680 ± 160
3	740 ± 150	200 ± 50	700 ± 140	760 ± 150
4	850 ± 140	230 ± 50	810 ± 140	900 ± 140
5	920 ± 140	230 ± 60	860 ± 150	970 ± 140
6	970 ± 150	210 ± 50	940 ± 160	1020 ± 140
7	1060 ± 160	180 ± 60	1030 ± 160	1100 ± 160
8	1140 ± 150	180 ± 50	1110 ± 150	1150 ± 140
9	1160 ± 150	180 ± 40	1130 ± 140	1170 ± 150
10	1120 ± 190	230 ± 80	1090 ± 160	1180 ± 190
b: Lower slice #				
1	970 ± 120	330 ± 40	890 ± 120	1070 ± 130
2	1010 ± 120	310 ± 50	960 ± 110	1120 ± 150
3	1040 ± 110	290 ± 50	970 ± 110	1130 ± 120
4	1160 ± 120	270 ± 50	1120 ± 110	1190 ± 120
5	1140 ± 140	290 ± 80	1090 ± 150	1190 ± 110
6	1140 ± 140	280 ± 70	1090 ± 140	1200 ± 140
7	1220 ± 140	250 ± 70	1170 ± 140	1260 ± 140
8	1300 ± 150	240 ± 70	1260 ± 150	1330 ±150
9	1390 ± 130	230 ± 60	1330 ± 130	1430 ± 130
10	1430 ± 180	230 ± 60	1400 ± 180	1490 ± 190

[a]In milliseconds; SD, group standard deviation.

values were calculated for the gray and white matter, respectively (Table 1). For the upper part of the brain, the mean white matter ATT was 64 ms longer than that of the gray matter; for the lower part, the difference was 111 ms. Per-subject pairwise t tests showed that these differences in ATT between the gray and white matter were significant ($P < 0.05$).

Empiric ATT values are usually assumed on a per-slice basis when CBF is quantified using ASL. For instance, in flow-sensitive alternating inversion recovery (FAIR) perfusion imaging, especially single-slice FAIR (36,37), the ATT value is assumed to be very small so it is set to 0. In QUIPSS II (10,12), TI_1 takes the place of TI-τ_a in Eq. 1, i.e., $\tau_a = TI - TI_1$. Linear regression lines for the in-slice mean ATT values were plotted for both the upper and the lower parts of the brain, as compared with that assumed in QUIPSS II (Fig. 3a). The in-slice ATT spatial SD is plotted in Fig. 3b.

In order to appreciate the errors caused in ASL CBF measurements that use empiric ATT values on a per-slice basis and ignore in-slice spatial variations and their dependence on the imaging location, CBF was quantified using the ASL model (Eqs. 1 and 2) by assuming different ATT values: (1) the in-slice mean ATT estimated in this study (group average, Fig. 3a); and (2) the ATT values indicated by the QUIPSS II model. For our study, $\tau_a(i) = 1400 + 55 \times (i - 1) - 700$ ms. The CBF calculated in this manner was then compared with that measured by PET, and the results are shown in Fig. 4 and Table 2.

In the activation studies, within both the sensorimotor and visual ROIs (Fig. 5), ΔM, CBF, and ATT were estimated for both the resting and activated states, and the task-induced changes in each of these parameters were calculated (Table 3). The reduction in the ATT due to focal activation was of similar magnitude for both the visual and motor tasks (~80 ms). This result indicates that, within the visual ROI, when quantified by ignoring

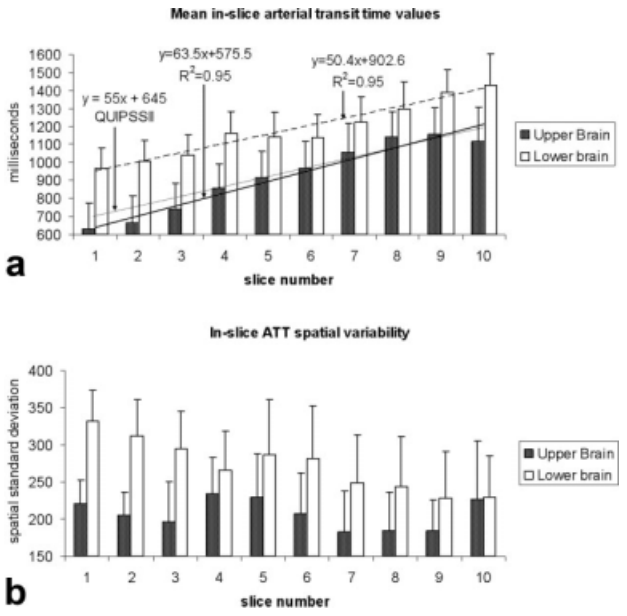

FIG. 3. In-slice mean ATT values on a per-slice basis **(a)** and the in-slice ATT spatial variability **(b)** for the upper and lower parts of the brain. The linear regression lines and equations of the ATT values are shown. For comparison, the line of ATT values assumed in QUIPSS is also plotted, whose slope is dependent on the data acquisition duration of each slice. Error bars indicate the standard deviations in the group analysis.

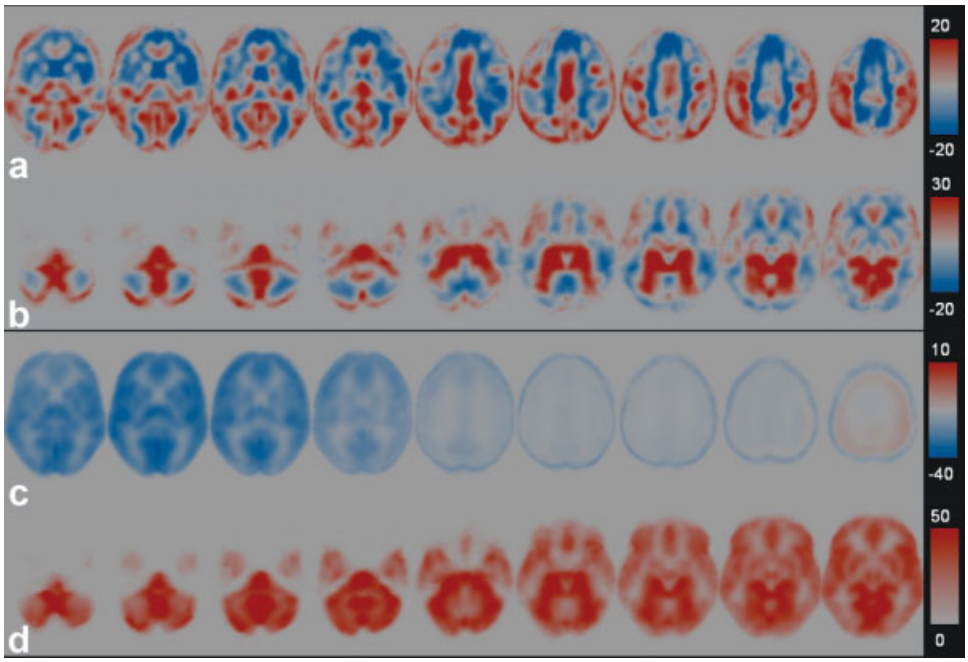

FIG. 4. ASL CBF was first calculated using the mean slice-based ATT values estimated in this study and then compared to CBF measured by PET. The voxelwise differences are shown in **(a)** for the upper part of the brain and in **(b)** for the lower part. **c,d:** The differences between CBF quantified using the QUIPSS II model and that measured by PET.

the task-induced changes in ATT, the increase in task-induced CBF would be 44% of the baseline value, whereas taking into account changes in ATT reduced the increase to 23% of the baseline CBF value. In the sensorimotor ROI, these numbers were 40% and 25%, respectively.

DISCUSSION

ATTs were calculated on a per-voxel basis based on the ASL-MRI, and PET data were collected in the same group of subjects. Spatial variations of the ATTs and their dependence on the ASL geometry were examined in terms of imaging location, the gap between the

Table 2
ASL CBF Values were Calculated for Both the Upper **(a)** and Lower **(b)** Acquisition Slabs in the Brain, Using the ATT Values on a Per-Slice Basis that were Either Estimated (see Table 1, 2nd Column) or Assumed in QUIPSS II (see Fig. 3a), and These were Compared with Those Measured by PET (Shown in the 2nd Column from Left Under PET). The Mean In-Slice CBF Values Calculated Using the Mean Slice-Based ATT Values are Shown Under ASL_m in the 3rd Column from Left, and the Differences Between the ASL and PET CBF Values is Listed in the 2nd Column from the Right (ASL_m-PET). Similarly, the Mean In-Slice CBF Values Estimated by ASL Using QUIPSS II are Listed Under ASL_q in the 4th Column from Left, and the Differences Between the ASL and PET CBF Data are Shown in the Right-Most Column (ASL_q-PET)

	PET	ASL_m	ASL_q	ASL_m-PET	ASL_q-PET
a: Upper slice #					
1	39.7	40.6	44.6	0.9	4.9*
2	40.7	41.5	46.7	0.8	6.0*
3	39.6	39.9	44.0	0.4	4.4*
4	39.1	40.4	41.0	1.4	2.0
5	41.4	42.9	43.1	1.5	1.6
6	43.8	44.2	44.8	0.3	0.9
7	43.6	44.4	42.6	0.8	−1.1
8	41.1	41.0	37.8	0.0	−3.3
9	39.0	38.7	35.8	−0.3	−3.2
10	34.3	33.2	36.8	−1.1	2.6
b: Lower slice #					ASL_q-PET*
1	32.2	33.0	20.5	0.9	−11.6
2	35.5	37.3	24.0	1.8	−11.5
3	38.4	38.2	25.5	−0.1	−12.9
4	39.8	40.2	24.7	0.4	−15.1
5	41.5	42.3	28.8	0.8	−12.7
6	42.8	42.8	31.4	−0.1	−11.4
7	42.8	43.8	31.6	1.0	−11.2
8	42.2	43.9	30.4	1.7	−11.8
9	41.0	40.6	26.1	−0.4	−14.9
10	39.7	41.2	27.5	1.5	−12.2

*CBF unit mL/100 g/min; $P < 0.001$.

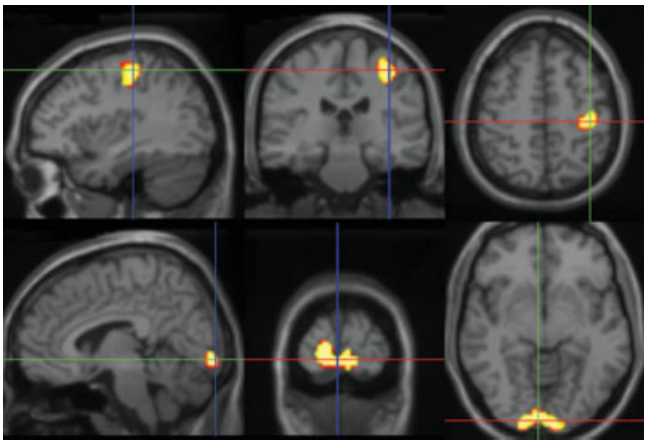

FIG. 5. ROIs defined based on PET CBF activations.

imaging and labeling slabs, the order of slices, and functional activation. CBF was calculated using the ATT values optimized for each slice in one instance and using those assumed in the QUIPSS II model in another. The CBF values from these two calculations were then compared with those obtained using PET. The task-induced changes in the ATT values within the sensorimotor and visual ROIs were also estimated.

The map of the ASL perfusion-induced signal changes (ΔM) shows some similarity to the CBF map (f_{PET}) measured by PET (Figs. 1 and 2). The contamination from the intravascular blood signal around the cerebral arteries can be seen in the MR intensity difference maps (ΔM) for the lower imaging slab (top row, Fig. 2). The ATT map obtained in this study shows a very similar pattern to those of the bolus arrival time estimates with the dynamic susceptibility contrast method (38). However, susceptibility artifacts around the frontal sinus are seen in most of the inferior slices acquired from the lower part of the brain due to the narrow bandwidth in the phase-encoding direction. Efforts have been made in postprocessing to reduce the influence of these effects on our observations: first, nonlinear image registration strategies proposed by Duncan et al. (39) were implemented and employed to improve the (co)registration accuracy and to reduce the geometric distortions; and second, ROIs were selected based on the group average BOLD images that excluded the ATT values from these problematic regions, especially in the inferior slices (see the ATT/τ_a maps in Figs. 1 and 2).

The results of this study show that ASL imaging for the lower part of the brain had significantly longer ATTs than for the upper part, with an average increase of 260 $\pm$ 20 (standard error of the mean) ms. It should be noted that the only difference in imaging parameters for the upper and lower sections was the location of the labeling and imaging slabs; the difference was a 54 mm downward displacement. The causes of this paradoxical observation are not obvious. It may relate to a change in the flow pathways in the large arteries due to the downward displacement of the labeling region. For example, it takes longer for the labeled arterial blood in large arteries to reach capillaries than that in small arteries or arterioles. When the labeling location is low, more large arteries are likely labeled due to the "tree-like" structure of the arterial blood delivery system.

In this study, slices 1, 2, 3, and 4 of the upper slab had the same brain coverage as slices 7, 8, 9, and 10 of the lower slab, which allowed us to assess the ASL imaging timing in terms of the gap between the imaging slab and the labeling slab. For the upper slab, the gap between the first slice and the labeling slab was 20 mm and the mean ATT to the first slice was 630 $\pm$ 30 ms; for the lower slab, the gap between the 7th slice and the labeling slab was 74 mm and the average ATT to the 7th was 1220 $\pm$ 30 ms. Over all four slices, the mean difference was 610 $\pm$ 20 ms. These results show that any change in the gap between the imaging and labeling slabs will change the ATT values dramatically and could have a marked effects on CBF quantification. It should be noted that slice 7 in the lower acquisition may also be influenced by the data acquisition process for the first six slices, but assuming these effects are small, the only factor that was changed between the two acquisitions of these slices was a difference in gap of 54 mm between the imaging and labeling slabs. This change in ATT values as a function of a change in the gap between the label and the imaging locations also allows us to estimate a mean arterial blood velocity of 8.8 cm/sec.

Marked spatial variability existed in the ATT within slices (Fig. 3b; Table 1). The mean spatial SD was 210 for the upper part and 270 for the lower part of the brain. When the per-slice ATT values are used in ASL CBF quantification, for the upper part of the brain, for example, this means over 37% of the voxels were underestimated by at least 20% or overestimated by at least 34% of the CBF value measured by PET. The lower part of the brain exhibited more spatial variability. This was likely attributable to contributions of residual signals from large arteries that were not completely suppressed by the applied crusher gradients.

The segmentation-based results revealed that the mean ATT for the white matter over the slabs examined was significantly longer than that of the gray matter for both the lower and upper parts of the brain ($P < 0.05$, per-subject pairwise t test). The mean differences in ATT between the white and gray matter are slightly smaller than the differences in the TA (time of appearance)

Table 3
Task-Induced Changes in ΔM, CBF, and ATT With Both the Sensorimotor **(a)** and Visual **(b)** ROIs

	ASL ΔM	PET CBF	ATT
a: Motor ROI			
Rest state	2.06 $\pm$ 0.13	41.3 $\pm$ 1.7	904.0
Finger tap	2.88 $\pm$ 0.17	51.8 $\pm$ 1.6	821.2
Difference	0.82 $\pm$ 0.06*	10.5 $\pm$ 1.1*	−82.8
b: Visual ROI			
Rest state	1.35 $\pm$ 0.12	48.2 $\pm$ 1.9	1251.5
CB	1.94 $\pm$ 0.17	56.9 $\pm$ 1.9	1170.0
Difference	0.59 $\pm$ 0.09	8.6 $\pm$ 1.1*	−81.5

PET CBF is in mL/100 g/min, ASL ΔM in a.u., and ATT in milliseconds; CB: checkerboard; *$P < 0.05$.

values obtained by dynamic susceptibility contrast MRI (40,41). We had hoped that the gray matter (GM) and white matter (WM) differences in ATT would explain most of the spatial variability we observed in this study. But the ATT spatial variability based on GM-WM segmentation turned out to be similar in magnitude to that without segmentation. One most likely explanation of this observation is that the ATT spatial variability is more dependent on the anatomy of the brain vasculature than brain tissue classification.

Using the in-slice mean ATT values listed in Table 1, CBF was quantified using Eq. 1 and was compared with that measured by PET. This comparison allowed us to estimate the spatial variability in ASL CBF quantification caused by ignoring the in-slice ATT spatial variability. For the upper part of the brain, the error in ASL CBF could be as much as 20 mL/100 g/min; for the lower section, it was up to 30 mL/100 g/min. CBF was also calculated using the ATT values assumed in QUIPPS II and was compared with that by PET, and differences up to 50 mL/g/min were observed in voxels. The in-slice mean CBF values were significantly different for all slices of the lower part (Table 2b; $P < 0.001$) and for some of the slices of the upper part (Table 2a; $P < 0.05$). The QUIPSS II model assumes a linear relationship between the ATT and the slice number. The data presented here indicate good agreement with the QUIPSS II model for the upper part of the brain; the QUIPSS line is close to the regression line of the upper part but far away from the regression line of the lower part, with a slope of 55 ms/slice falling in between those of the two lines. In practice, the slope of the QUIPSS II line can be adjusted by changing the width of the echo-planar imaging data acquisition time window.

The reduction in ATT due to focal activation was of similar magnitude for both the visual and motor tasks (~80 ms) and lower than that reported in a previous sensorimotor study (~110 ms) by Yang et al. (17), in which pulsed ASL was used with a range of TIs. In another sensorimotor and visual study (19), ATT was determined by continuous ASL, to decrease by approximately 150 ms upon activation. Hendrikse et al. (24) reported a decrease of ATT <100 ms in response to visual stimulation. The ATT changes measured using turbo-continuous ASL were much higher (13).

A detailed discussion of ATT effects and optimization of ASL imaging parameters in terms of the ATT can be found in (25,42). Insights from this study provide researchers with more specific information of factors to be considered in comparing ASL CBF results across studies. The data presented here can also be used to further optimize the ASL imaging parameters. The two-part ASL acquisition used in this study allows us to examine the dependence of the ATT effects on the slice thickness, labeling position, and the gap between the imaging and the labeling slabs. To the best of our knowledge, this is the first study to address these issues systematically. For any functional study using ASL on normal subjects at 3 T, the group average ATT maps can be used on a per-voxel basis to minimize the errors in absolute CBF quantification, provided that all the imaging parameters are identical to those employed in this study, including slice location and orientation. Under circumstances that the imaging parameters change, the results presented here could still be used to generate a set of relative ATTs on a per-slice basis, which could be accomplished by extending the results obtained in this study to take into account the changes in specific imaging parameters and/or geometry.

The TR was set to 2 sec in this study so that more perfusion images could be collected within a given the total scan time. When the ATT is very long, for example, as could be the case in neonates or patients (43), the bolus "aliasing" between TRs could result in negative signal intensity changes. All subjects recruited in the study were normal and healthy adults and no negative ASL signal due to bolus aliasing was observed.

The intravascular flow crusher gradient was set to $V_{enc} = 5$ cm/sec, which was a compromise among several considerations: the gradient was large enough to suppress the intravascular flow contamination, and it was applied within the magnetic resonance safety limits while also allowing for a fairly short echo time to avoid imaging artifacts induced by spin-spin relaxation (44).

In the assessment of the effects of the ATT spatial variability on ASL CBF quantification, we assumed that the ATT spatial variability was the major source of error. There are other factors not measured that could contribute to the observed CBF quantification errors, such as the brain-blood water partition coefficient (λ) and the RF labeling efficiency (α_π). Bolus dispersion might also occur in some voxels (45). However, neither of these effects would be expected to vary systematically as a function of slice location and acquisition order, and thus we can assume these unmeasured parameters were not influencing the results presented.

[^{15}O]water PET imaging is a time-honored technique that is considered to be the current standard in human CBF measurements, and we have incorporated the most recently developed techniques in PET CBF quantification (46). The construction of high-resolution research tomograph is designed to minimize partial-volume effects, with the potential for extremely high resolution (<3 mm) for human and large-animal brain imaging. The use of phoswich detectors (10 mm lutetium oxyorthosilicate and lutetium yttrium orthosilicate scintillator detectors) provides the capability to achieve excellent uniformity in resolution across the field of view. The small aperture (46.9-cm diameter), long axial field of view (25.2 cm), and 20 mm crystal depth provides high sensitivity, allowing sufficient counts so that images with high resolution can have reasonable statistical quality. In this study, PET images had a high reconstructed resolution of ~2.5 mm to minimize partial-volume effects.

Donahue et al. (47) have examined CBF measured with the transfer insensitive labeling technique (TILT) as a function of spatial resolution and postlabeling delay times and compared it with CBF values from the PET literature. They found that when the ASL acquisition resolution increased from $3.75 \times 3.75 \times 3$ mm^3 to $7.5 \times 7.5 \times 3$ mm^3, the CBF value within an occipital gray matter ROI decreased up to 15.4% due to the partial-volume effect, as quantified with a one-compartment model. Based on their data, the decrease in CBF (within the same gray matter ROI) due to the partial-volume effect with an acquisition resolution of $4 \times 4 \times 6$ mm^3 should be <12%. When both the gray and white matter are

considered within a slice, the mean in-slice ATTs should be much less affected.

Although [O-15]water PET has been used as the gold standard in measuring CBF, it may give erroneously lower values in high-flow regions due to limited extraction. Within these regions, the method we used to estimate ATT in this study will also yield biased values.

CONCLUSIONS

In most of the previous comparisons of PET and MRI in quantifying CBF, data from the two modalities were directly compared (47–51). In this study, the PET data were instead used to inform the MR data to reveal the effects of ATTs on the quantitative CBF obtained using ASL-MRI. This allowed us to investigate ATT effects on a per-voxel and per-slice basis across the whole brain. The data also allowed an examination of the dependence of ATT values on the location of the imaging slab and the gap between the imaging and labeling slab and the resultant errors in ASL CBF quantification as a function of these factors. Task-induced decreases in ATT within sensorimotor and visual cortex were also calculated, and their effect on CBF quantification was revealed. The observations in this study provide researchers with the necessary information to set up ASL imaging parameters and to use the appropriate ATT values to minimize errors in absolute CBF quantification.

ACKNOWLEDGMENTS

This work was supported in part by Pfizer. We appreciate the excellent technical contributions of the staff of the Yale PET and MR Centers. We thank Jennifer Roth and Jason Stockmann for their helpful advice on an earlier version of the manuscript.

APPENDIX

The ATT τ_a was estimated on a per-voxel basis using the following iterative algorithm:

Step 1: Set $c\,(0) = 1$, $\tau_a\,(0) = 0$, and $i = 1$;

Step 2: Calculate $\tau_a\,[i]$ as follows:

$$\tau_a[i] = TI - \frac{\lambda \Delta M(TI) e^{TI/\mathrm{T}_{1a}}}{2c[i-1] f_{PET} M_0}$$

Step 3: If $|\tau_a[i] - \tau_a[i-1]|/\tau_a[i] < \xi$ or $i > \mathrm{N}_{\max}$, go to step 4; otherwise, estimate c[i] according to the following equation:

$$c(i) = \alpha_\pi \frac{1 - e^{-(TI-\tau_a)(1/T_{1app} - 1/T_{1a})}}{(TI - \tau_a(i))(1/T_{1app} - 1/T_{1a})}$$

i = $i + 1$; go to step 2;

Step 4: Select next voxel; go to step 1.

In this study, we chose $\xi = 0.001$ and $\mathrm{N}_{\max} = 500$. Other perfusion-related parameters used in ATT quantification: $T_{1\mathrm{a}} = 1490$ ms, $\lambda = 0.9$ mL/g, and $\alpha_\pi = 0.95$ (3).

REFERENCES

1. Lipton ML, Branch CA, Hrabe J, Lewis DP, Helpern JA. RF excitation profiles with FAIR: impact of truncation of the arterial input function on quantitative perfusion. J Magn Reson Imaging 2001;13:207–214.
2. Yongbi MN, Yang Y, Frank JA, Duyn JH. Multislice perfusion imaging in human brain using the C-FOCI inversion pulse: comparison with hyperbolic secant. Magn Reson Med 1999;42:1098–1105.
3. Zhan W, Gu H, Silbersweig DA, Stern E, Yang Y. Inversion profiles of adiabatic inversion pulses for flowing spins: the effects on labeling efficiency and labeling accuracy in perfusion imaging with pulsed arterial spin-labeling. Magn Reson Imaging 2002;20:487–494.
4. Frank LR, Wong EC, Buxton RB. Slice profile effects in adiabatic inversion: application to multislice perfusion imaging. Magn Reson Med 1997;38:558–564.
5. Moller HE, Mildner T, Preul C, Zimmer C, von Cramon DY. Assessment of collateral supply by two-coil continuous arterial spin labeling after coil occlusion of the internal carotid artery. AJNR Am J Neuroradiol 2007;28:1304–1305.
6. Zhang X, Nagaoka T, Auerbach EJ, Champion R, Zhou L, Hu X, Duong TQ. Quantitative basal CBF and CBF fMRI of rhesus monkeys using three-coil continuous arterial spin labeling. Neuroimage 2007; 34:1074–1083.
7. Talagala SL, Ye FQ, Ledden PJ, Chesnick S. Whole-brain 3D perfusion MRI at 3.0 T using CASL with a separate labeling coil. Magn Reson Med 2004;52:131–140.
8. Mildner T, Trampel R, Moller HE, Schafer A, Wiggins CJ, Norris DG. Functional perfusion imaging using continuous arterial spin labeling with separate labeling and imaging coils at 3 T. Magn Reson Med 2003;49:791–795.
9. Zaharchuk G, Ledden PJ, Kwong KK, Reese TG, Rosen BR, Wald LL. Multislice perfusion and perfusion territory imaging in humans with separate label and image coils. Magn Reson Med 1999;41:1093–1098.
10. Wong EC, Buxton RB, Frank LR. Quantitative imaging of perfusion using a single subtraction (QUIPSS and QUIPSS II). Magn Reson Med 1998;39:702–708.
11. Alsop DC, Detre JA. Reduced transit-time sensitivity in noninvasive magnetic resonance imaging of human cerebral blood flow. J Cereb Blood Flow Metab 1996;16:1236–1249.
12. Luh WM, Wong EC, Bandettini PA, Hyde JS. QUIPSS II with thin-slice TI1 periodic saturation: a method for improving accuracy of quantitative perfusion imaging using pulsed arterial spin labeling. Magn Reson Med 1999;41:1246–1254.
13. Hernandez-Garcia L, Lee GR, Vazquez AL, Yip CY, Noll DC. Quantification of perfusion fMRI using a numerical model of arterial spin labeling that accounts for dynamic transit time effects. Magn Reson Med 2005;54:955–964.
14. Mildner T, Moller HE, Driesel W, Norris DG, Trampel R. Continuous arterial spin labeling at the human common carotid artery: the influence of transit times. NMR Biomed 2005;18:19–23.
15. Thomas DL, Lythgoe MF, van der Weerd L, Ordidge RJ, Gadian DG. Regional variation of cerebral blood flow and arterial transit time in the normal and hypoperfused rat brain measured using continuous arterial spin labeling MRI. J Cereb Blood Flow Metab 2006;26:274–282.
16. Zhou J, van Zijl PC. Effect of transit times on quantification of cerebral blood flow by the FAIR T(1)-difference approach. Magn Reson Med 1999;42:890–894.
17. Yang Y, Engelien W, Xu S, Gu H, Silbersweig DA, Stern E. Transit time, trailing time, and cerebral blood flow during brain activation: measurement using multislice, pulsed spin-labeling perfusion imaging. Magn Reson Med 2000;44:680–685.
18. Wang J, Alsop DC, Song HK, Maldjian JA, Tang K, Salvucci AE, Detre JA. Arterial transit time imaging with flow encoding arterial spin tagging (FEAST). Magn Reson Med 2003;50:599–607.
19. Gonzalez-At JB, Alsop DC, Detre JA. Cerebral perfusion and arterial transit time changes during task activation determined with continuous arterial spin labeling. Magn Reson Med 2000;43:739–746.
20. Li KL, Zhu X, Hylton N, Jahng GH, Weiner MW, Schuff N. Four-phase single-capillary stepwise model for kinetics in arterial spin labeling MRI. Magn Reson Med 2005;53:511–518.
21. MacIntosh BJ, Pattinson KT, Gallichan D, Ahmad I, Miller KL, Feinberg DA, Wise RG, Jezzard P. Measuring the effects of remifentanil on cerebral blood flow and arterial arrival time using 3D GRASE MRI with pulsed arterial spin labelling. J Cereb Blood Flow Metab 2008; 28:1514–1522.

22. Petersen ET, Lim T, Golay X. Model-free arterial spin labeling quantification approach for perfusion MRI. Magn Reson Med 2006;55: 219–232.
23. Barbier EL, Silva AC, Kim HJ, Williams DS, Koretsky AP. Perfusion analysis using dynamic arterial spin labeling (DASL). Magn Reson Med 1999;41:299–308.
24. Hendrikse J, Lu H, van der Grond J, Van Zijl PC, Golay X. Measurements of cerebral perfusion and arterial hemodynamics during visual stimulation using TURBO-TILT. Magn Reson Med 2003;50:429–433.
25. Xie J, Gallichan D, Gunn RN, Jezzard P. Optimal design of pulsed arterial spin labeling MRI experiments. Magn Reson Med 2008;59: 826–834.
26. Freeman AJ, Gowland PA, Mansfield P. Optimization of the ultrafast Look-Locker echo-planar imaging T1 mapping sequence. Magn Reson Imaging 1998;16:765–772.
27. Braun AR, Balkin TJ, Wesenten NJ, Carson RE, Varga M, Baldwin P, Selbie S, Belenky G, Herscovitch P. Regional cerebral blood flow throughout the sleep-wake cycle. An H2(15)O PET study. Brain 1997;120(pt 7):1173–1197.
28. Aguirre GK, Detre JA, Zarahn E, Alsop DC. Experimental design and the relative sensitivity of BOLD and perfusion fMRI. Neuroimage 2002;15:488–500.
29. Wong EC, Buxton RB, Frank LR. Implementation of quantitative perfusion imaging techniques for functional brain mapping using pulsed arterial spin labeling. NMR Biomed 1997;10:237–249.
30. Wang J, Aguirre GK, Kimberg DY, Roc AC, Li L, Detre JA. Arterial spin labeling perfusion fMRI with very low task frequency. Magn Reson Med 2003;49:796–802.
31. Andersson JL, Vagnhammar BE, Schneider H. Accurate attenuation correction despite movement during PET imaging. J Nucl Med 1995; 36:670–678.
32. Iida H, Higano S, Tomura N, Shishido F, Kanno I, Miura S, Murakami M, Takahashi K, Sasaki H, Uemura K. Evaluation of regional differences of tracer appearance time in cerebral tissues using [^{15}O] water and dynamic positron emission tomography. J Cereb Blood Flow Metab 1988;8:285–288.
33. Herscovitch P, Markham J, Raichle ME. Brain blood flow measured with intravenous H2(15)O, I: theory and error analysis. J Nucl Med 1983;24:782–789.
34. Papademetris X, Jackowski AP, Schultz RT, Staib LH, Duncan JS.Integrated intensity and point-feature nonrigid registration. In: Medical Image Computing and Computer-Assisted Intervention, Miccai, 2004, Pt 1. p 763–770.
35. Forman SD, Cohen JD, Fitzgerald M, Eddy WF, Mintun MA, Noll DC. Improved assessment of significant activation in functional magnetic resonance imaging (fMRI): use of a cluster-size threshold. Magn Reson Med 1995;33:636–647.
36. Kim SG. Quantification of relative cerebral blood flow change by flow-sensitive alternating inversion recovery (FAIR) technique: application to functional mapping. Magn Reson Med 1995;34:293–301.
37. Kim SG, Tsekos NV, Ashe J. Multi-slice perfusion-based functional MRI using the FAIR technique: comparison of CBF and BOLD effects. NMR Biomed 1997;10:191–196.
38. Duyn JH, van Gelderen P, Talagala L, Koretsky A, de Zwart JA. Technological advances in MRI measurement of brain perfusion. J Magn Reson Imaging 2005;22:751–753.
39. Duncan JS, Papademetris X, Yang J, Jackowski M, Zeng X, Staib LH. Geometric strategies for neuroanatomic analysis from MRI. Neuroimage 2004;23(suppl 1):S34–45.
40. Kluytmans M, van der Grond J, Viergever MA. Gray matter and white matter perfusion imaging in patients with severe carotid artery lesions. Radiology 1998;209:675–682.
41. Kluytmans M, van der Grond J, Folkers PJ, Mali WP, Viergever MA. Differentiation of gray matter and white matter perfusion in patients with unilateral internal carotid artery occlusion. J Magn Reson Imaging 1998;8:767–774.
42. Wong EC, Buxton RB, Frank LR. A theoretical and experimental comparison of continuous and pulsed arterial spin labeling techniques for quantitative perfusion imaging. Magn Reson Med 1998;40: 348–355.
43. Wang J, Licht DJ, Silvestre DW, Detre JA. Why perfusion in neonates with congenital heart defects is negative: technical issues related to pulsed arterial spin labeling. Magn Reson Imaging 2006;24: 249–254.
44. St Lawrence KS, Wang J. Effects of the apparent transverse relaxation time on cerebral blood flow measurements obtained by arterial spin labeling. Magn Reson Med 2005;53:425–433.
45. Gallichan D, Jezzard P. Modeling the effects of dispersion and pulsatility of blood flow in pulsed arterial spin labeling. Magn Reson Med 2008;60:53–63.
46. Wienhard K, Eriksson L, Eriksson M, Casey ME, Knoess C, Bruckbauer T, Hamill J, Schmand M, Gremillion T, Lenox A, Conti M, Bendriem B, Heiss WD, Nutt R. The ECAT HRRT: NEMA NEC evaluation of the HRRT system, the new high resolution research tomograph. In: 2001 IEEE Nuclear Science Symposium, San Siego, CA. Conference Records, Vols 1–4, 2002. p 1227–1230, 2518.
47. Donahue MJ, Lu H, Jones CK, Pekar JJ, van Zijl PC. An account of the discrepancy between MRI and PET cerebral blood flow measures. A high-field MRI investigation. NMR Biomed 2006;19:1043–1054.
48. Chen JJ, Wieckowska M, Meyer E, Pike GB. Cerebral blood flow measurement using fMRI and PET: a cross-validation study. Int J Biomed Imaging 2008;2008:516359.
49. Carroll TJ, Teneggi V, Jobin M, Squassante L, Treyer V, Hany TF, Burger C, Wang L, Bye A, Von Schulthess GK, Buck A. Absolute quantification of cerebral blood flow with magnetic resonance, reproducibility of the method, and comparison with H2(15)O positron emission tomography. J Cereb Blood Flow Metab 2002;22:1149–1156.
50. Ye FQ, Berman KF, Ellmore T, Esposito G, van Horn JD, Yang Y, Duyn J, Smith AM, Frank JA, Weinberger DR, McLaughlin AC. H(2)(15)O PET validation of steady-state arterial spin tagging cerebral blood flow measurements in humans. Magn Reson Med 2000;44: 450–456.
51. Feng CM, Narayana S, Lancaster JL, Jerabek PA, Arnow TL, Zhu F, Tan LH, Fox PT, Gao JH. CBF changes during brain activation: fMRI vs. PET. Neuroimage 2004;22:443–446.